


# Nanoplasmonic amplification in microfluidics enables accelerated colorimetric quantification of nucleic acid biomarkers from pathogens

Received: 20 July 2022

Accepted: 22 March 2023

Published online: 1 June 2023

 Check for updates

Tamer AbdElFatah <sup>1,8</sup>, Mahsa Jalali <sup>1,8</sup>, Sripadh Guptha Yedire <sup>1</sup>, Imman I. Hosseini <sup>1</sup>, Carolina del Real Mata <sup>1</sup>, Haleema Khan<sup>1</sup>, Seyed Vahid Hamidi <sup>1</sup>, Olivia Jeanne<sup>1</sup>, Roozbeh Siavash Moakhar <sup>1</sup>, Myles McLean<sup>2,3</sup>, Dhanesh Patel <sup>4,5</sup>, Zhen Wang <sup>2,3</sup>, Geoffrey McKay <sup>6</sup>, Mitra Yousefi <sup>4</sup>, Dao Nguyen <sup>6,2</sup>, Silvia M. Vidal<sup>4,5</sup>, Chen Liang<sup>2,3</sup> & Sara Mahshid <sup>1,7</sup> ✉

Deployment of nucleic acid amplification assays for diagnosing pathogens in point-of-care settings is a challenge due to lengthy preparatory steps. We present a molecular diagnostic platform that integrates a fabless plasmonic nano-surface into an autonomous microfluidic cartridge. The plasmonic ‘hot’ electron injection in confined space yields a ninefold kinetic acceleration of RNA/DNA amplification at single nucleotide resolution by one-step isothermal loop-mediated and rolling circle amplification reactions. Sequential flow actuation with nanoplasmonic accelerated microfluidic colorimetry and in conjugation with machine learning-assisted analysis (using our ‘QolorEX’ device) offers an automated diagnostic platform for multiplexed amplification. The versatility of QolorEX is demonstrated by detecting respiratory viruses: SARS-CoV-2 and its variants at the single nucleotide polymorphism level, H1N1 influenza A, and bacteria. For COVID-19 saliva samples, with an accuracy of 95% on par with quantitative polymerase chain reaction and a sample-to-answer time of 13 minutes, QolorEX is expected to advance the monitoring and rapid diagnosis of pathogens.

Molecular diagnosis based on polymerase chain reaction (PCR) strongly depends on lengthy protocols, costly reagents, complex equipment and highly trained staff<sup>1</sup>. In the context of the coronavirus disease 2019 (COVID-19) pandemic, the industry strove to develop assays that offer

multiple test results in a shorter time<sup>2,3</sup> (less than 1 h). However, sample preparation, nucleic acid extraction and detection are still hampered by long processing times<sup>4,5</sup>. In contrast to PCR, methods based on reverse transcription loop-mediated isothermal amplification (RT-LAMP) and

<sup>1</sup>Department of Bioengineering, McGill University, Montreal, Quebec, Canada. <sup>2</sup>Department of Medicine, McGill University, Montreal, Quebec, Canada.

<sup>3</sup>Lady Davis Institute for Medical Research and McGill Centre for Viral Diseases, Jewish General Hospital, Montreal, Quebec, Canada. <sup>4</sup>Department of Human Genetics, McGill University, Montreal, Quebec, Canada. <sup>5</sup>Dahdaleh Institute of Genomic Medicine, McGill University, Montreal, Quebec, Canada.

<sup>6</sup>Meakins-Christie Laboratories, Research Institute of the McGill University Health Centre, Montreal, Quebec, Canada. <sup>7</sup>Division of Experimental Medicine, McGill University, Montreal, Quebec, Canada. <sup>8</sup>These authors contributed equally: Tamer AbdElFatah, Mahsa Jalali. ✉e-mail: [sara.mahshid@mcgill.ca](mailto:sara.mahshid@mcgill.ca)

rolling circle amplification (RCA) are mainly capable of amplifying RNA/DNA in one step at a steady temperature<sup>6,7</sup>. Here, nucleic acid amplification releases H<sup>+</sup> ions that change the pH of the solution and the colour of the media in the presence of a pH-sensitive dye<sup>8,9</sup>. This hints at the potential of a quantitative versatile colorimetric read-out based on LAMP and RCA that can be leveraged for a point-of-care diagnosis system on par with quantitative PCR (qPCR). However, lack of sensitivity within a short turnaround time limits the translational application of colorimetric read-outs in clinical settings, despite their cost-effective operation and easy automation<sup>10,11</sup>. Recently, nanopatterned plasmonic nanostructures<sup>12–14</sup> enabled high optical absorption tunability across the visible spectrum due to resonance at unique light wavelengths, leading to a highly sensitive optical read-out<sup>10,15,16</sup>. The surface plasmon resonances of the free electrons harvest optical energy and form ‘hot’ electrons<sup>17,18</sup> that are capable of accelerating electro-photochemical catalytic reactions<sup>19–22</sup>. This unique characteristic of plasmonic nanopatterns, however, has not yet been investigated in the context of nucleic acid amplification testing.

To explore this possibility, we developed QolorEX, a point-of-care testing device analogous to qPCR that uniquely acquires the nanoplasmonic non-radiative relaxation of electron oscillations at nanolitre volumes to accelerate the one-step amplification in RT-LAMP and RCA and quantify the presence of nucleic acid biomarkers via colour reading at the level of single nucleotide polymorphism (SNP). The core principle of the QolorEX read-out is based on the unique combination of fabless self-assembly plasmonic sensing in a confined parallel microfluidic chamber, which results in hot electron injection from the surface of the nanoplasmonic sensor into the nanolitre volume of the media and ninefold enhancement in the kinetics of the amplification reaction (plasmonic hot-spot catalysis). We demonstrate that plasmonic-induced enhancement leads to expediting the nucleophilic reaction in the polymerization step of the amplification, which in turn results in the label-free pH-dependent colour transformation of phenol red from fuchsia to yellow in less than 10 minutes (min). To automate the sequential steps of the reaction, we developed a unique tunable angle-dependent actuation for precise spatial and temporal control over fluidic volumes and release of the reagents. Finally, we demonstrated this automation by tapping a button on a mobile phone application and using supervised machine learning-aided data analysis. Overall, the unique combination of versatile ultra-rapid enhanced nanoplasmonic sensing and autonomous multiplexed fluidic manipulation, as demonstrated by QolorEX, holds potential for easy access to diagnostic outcomes with a 13 min sample-to-answer turnaround time.

## Design and operation of the QolorEX system

The QolorEX device features two components that together present an automated, integrated and cost-effective approach to colorimetric amplification at the point-of-care or point-of-need (Fig. 1a and Supplementary Table 1): (1) The QolorEX imaging box is a portable battery-operated platform that consists of linear actuators and a motorized stage for automated sample processing, and an illumination-coupled imaging system that operates with a Bluetooth-interfaced smartphone application (Fig. 1b and

Supplementary Figs. 1 and 2). (2) The QolorEX microfluidic cartridge is a user-friendly platform with attached accessories for self-sample collection, reagent storage and flow actuation that automates the assay process when placed inside the imaging box. To enable multiplexing and avoid cross-chamber contamination during operation, the QolorEX microfluidic cartridge possesses triplicates of parallel fluidic modules. The cartridge equips a three-dimensional (3D)-printed cassette (Fig. 1c) that integrates a funnel for saliva collection (i) and a heating lysis chamber to lyse saliva at 95 °C for 3 min (ii; Fig. 1c, step 1 and Supplementary Fig. 3) and two submillimetre-sized thin elastomeric suction cups (iii and iv) that work in tandem to create a tunable negative pressure in steps of 30° rotations for timely release of reagents and mixing with the saliva at a 1:10 volume ratio (Fig. 1c, step 2 and Supplementary Fig. 4). The integrated elements heat the cartridge to 65 °C for 10 min to initiate the amplification reaction (Fig. 1c, step 3 and Supplementary Figs. 4f and 5). Finally, the illumination system acquires the images of the plasmonic colour-sensing chamber. This chamber (1.94 mm × 1.5 mm × 50 µm) is composed of four functional components: a plasmonic active aluminium (Al) layer as an electron release interface, a biocompatible back-scattering zinc oxide (ZnO) layer for bright plasmonic colour production, an array of closely packed organic nanoparticles to establish a honeycomb array with adjustable pitch and act as the spacer layer and finally, a silicon substrate with a large refractive index resulting in a high-intensity beam reflection (Fig. 1d). The rapidity and the quantified output of QolorEX strongly depend on the interaction between the nucleic acid amplification assay and the surface free electrons introduced by the plasmonic nanostructures. When the plasmonic nano-surface is irradiated with ambient light, the collective plasmonic oscillation of free electrons results in non-radiative relaxation in the form of hot electron injection into the media<sup>23,24</sup>, which can catalyse the electron-driven nucleic acid amplification at the interface of the plasmonic surface and the media (Supplementary Fig. 6). The electron emancipation at the interface of the plasmonic nano-surface facilitates the essential nucleic acid amplification step of the nucleophilic phosphodiester bond formation reaction<sup>25</sup> and consequently, increases the rate of this reaction (Fig. 1e). During the amplification reaction, protons that can be consumed by colour-changing chemical agents, such as phenol red, are generated to alter the refractive index of the media (Fig. 1f).

## Colorimetric signal generation and quantification in QolorEX

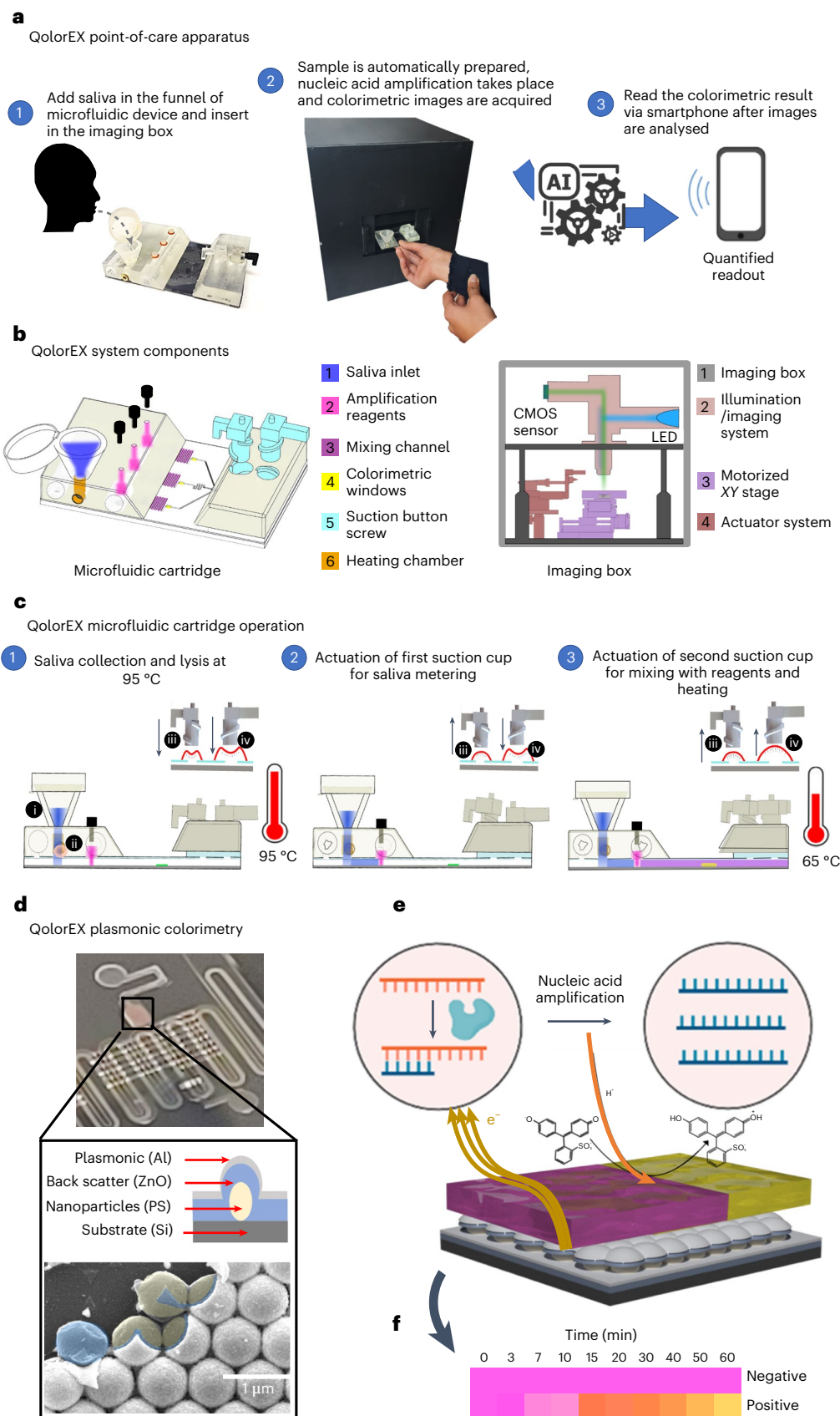
The QolorEX sensing chamber is designed to elicit plasmonic effects tuned by geometric and material parameters. Prior experimental and theoretical studies on plasmonic-based hot electron injection in aqueous media demonstrated enhanced multiphoton absorption that causes electron injection from the metal surface to the water<sup>20</sup>. In the confined medium of the sensing chamber (130 nl), the excess electrons accelerate the addition of new deoxynucleoside triphosphates to the primer tip where the α-phosphate groups act like electron acceptors<sup>25</sup> and increase the kinetics of the nucleophilic polymerization reaction. As a result, the release of H<sup>+</sup> ions and the pH-dependent colour change of the media from fuchsia to yellow in phenol red happens in less than 10 min (Fig. 2a).

**Fig. 1 | QolorEX rapid quantitative testing for point-of-care respiratory infection identification.** **a**, The rapid and point-of-care QolorEX identification of samples infected with a respiratory infection. **b**, The QolorEX system components include the microfluidic cartridge, which is embedded with a plasmonic test assay, a sample handling module and processing accessories for point-of-care operation (left). The QolorEX system also includes the imaging box for automated handling of the sequential amplification assay (right). CMOS, complementary metal–oxide–semiconductor. **c**, Microfluidic cartridge operation: In step 1, the user discharges the saliva into a funnel (i) housed on the microfluidic cartridge. Subsequently, the lysis chamber (a metal insert; ii) is heated to 95 °C for pathogen lysis. Following this, in step 2, the lysis chamber

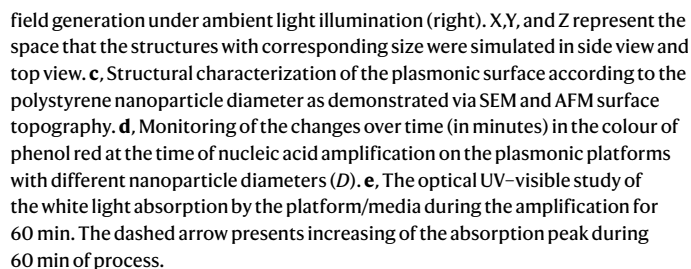
is vented to atmospheric pressure, and the lysed sample is suctioned to the Y-junction of the mixing module by actuating the first suction cup (iii). In the final step 3, the reagent storage chambers are vented and the second suction cup is actuated (iv) to engender mixing. **d**, The QolorEX plasmonic test chamber with a cross-section schematic and scanning electron microscopy (SEM) image illustrating the layered plasmonic substrate. PS, polystyrene. **e**, The chemical mechanism demonstrates the plasmonic-assisted rapid colorimetric read-out based on the indirect equilibrium shift of the phenol red redox reaction according to the altered kinetics of the nucleic acid amplification. **e**<sup>+</sup>, electron. **f**, The quantitative colour response of the QolorEX device in the absence and presence of the respiratory virus of interest.

To express plasmon resonance in large areas, fabless polystyrene nanoparticle self-assembly was used to construct the assemblies on biocompatible layered materials (Supplementary Figs. 7 and 8). The plasmonic free electron oscillation that leads to non-radiative

relaxation and determines the rate of free electron injection is directly correlated with the iridescence of light to activate plasmonic resonance<sup>26</sup>. To theoretically optimize the electromagnetic field enhancement of plasmonic platforms, we performed a series of numerical







electromagnetic field enhancement  $(|E|/|E_0|)^2$  of  $10^3$  times when illuminated with ambient light, where  $E_0$  is the electromagnetic field of the irradiated light and  $E$  is the surface-enhanced electromagnetic field. We experimentally investigated the pH-dependent colour change of phenol red for nanoparticles ranging from 100 nm to 750 nm as a result

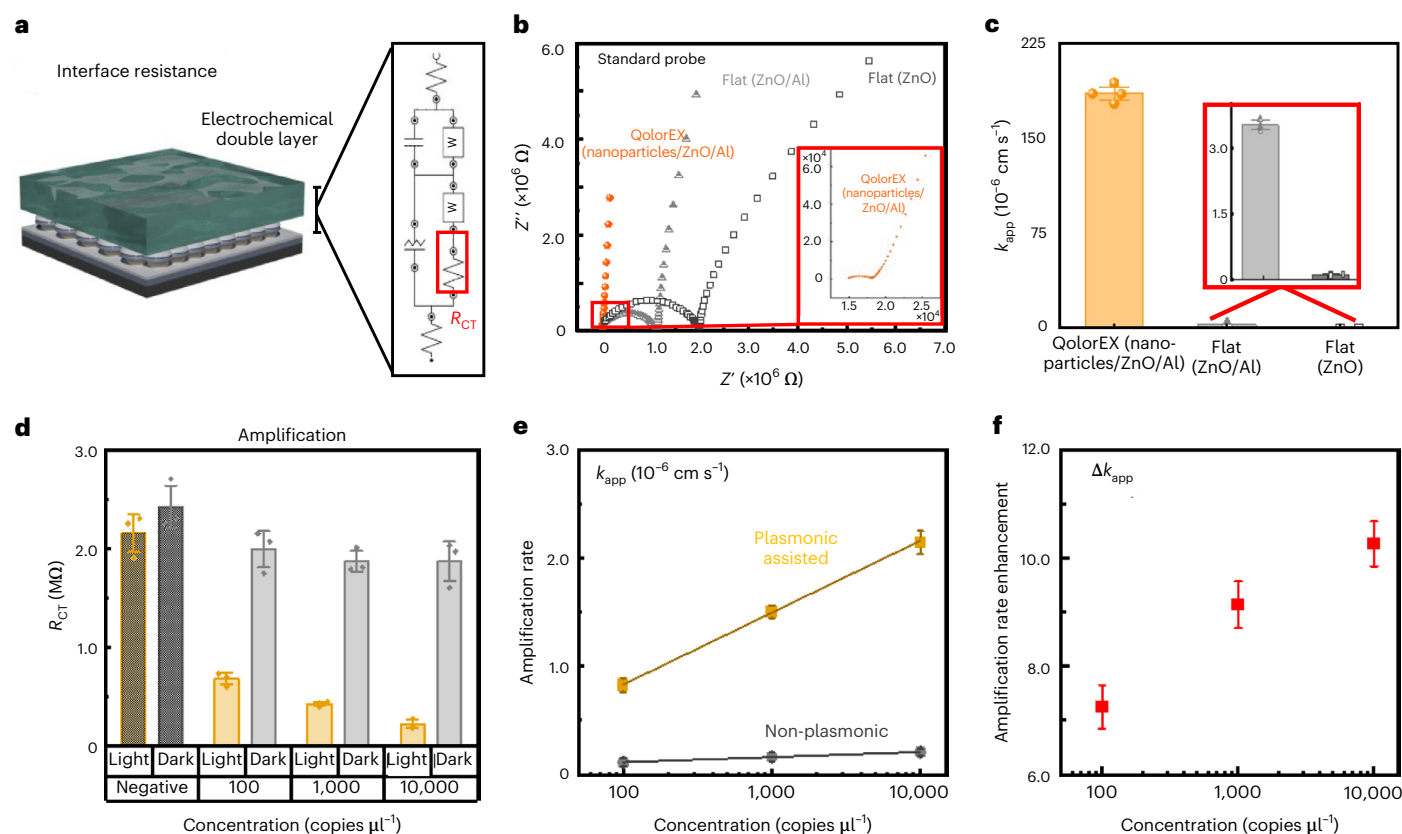


**Fig. 3 | Working principle of QolorEX plasmonic sensing platform with respect to RT-LAMP and RCA bioassays.** **a**, The study of the  $R_{CT}$  at the interface of the layered plasmonic QolorEX structures via impedimetric investigation of  $K_3FeCN_6$ . W, Warburg coefficient. **b**, Nyquist plots correlating with the impedimetric signal of the platform at different layer depositions.  $Z'$ , real part of impedance;  $Z''$ , imaginary part of impedance. **c**, Comparison of the calculated electron transfer rate constant at the interface of each layer in ambient light illumination based on  $R_{CT}$ . **d**, Electrochemical impedance spectroscopy

validation of the higher effect of electron injection under illumination in mitigation of the interface resistance with active LAMP assay in the presence of a target gene at different concentrations. **e**, Comparison of the calculated electron transfer rate constant at different target gene concentrations in ambient light illumination (plasmonic assisted) and a dark state (non-plasmonic) based on  $R_{CT}$ . **f**, The correlated nucleic acid amplification rate enhancement via QolorEX as a function of the target concentration. Data show mean values  $\pm$  standard error of the mean with a coefficient of 1.5 from three independent measurements.

of the nucleic acid amplification (Fig. 2d). To quantify the gamut of the colour change, we adopted a transduction signal based on the unique green component of the yellow colour, emphasized over the combination of the red and blue components in the fuchsia colour (equation (1)). Through the comparison of the transduction signal, we demonstrated that the plasmonic platform with a pitch of 400 nm presents a wider gamut of the media colour change. A complimentary UV–visible test was performed on the 400 nm plasmonic platform to illustrate the absorption wavelength variation over the gradual change of the media colour with a scaled acidity. This represents the time span of 60 min in the presence of the nucleic acid amplification assay (Fig. 2e).

$$\text{QolorEX signal} = \text{Green}^2 \cdot (\text{Red} \cdot \text{Blue})^{-1} \quad (1)$$

where Green, Red and Blue represent the intensity of each image channel, respectively.

To investigate the photo potential non-radiative relaxation and plasmonic catalysis of the nucleic acid amplification, we studied the kinetics of the reaction in the presence and absence of the emancipated plasmonic electrons via electrochemistry.

First, electrochemical impedance spectroscopy was used to study the surface resistance at the QolorEX plasmonic interface (polystyrene particles/ZnO/Al) under ambient light via a  $K_3FeCN_6$  (5 mM) standard probe (Fig. 3a). We quantified the enhanced electron transfer rate constant of QolorEX compared to the non-plasmonic layers of flat

ZnO/Al and flat ZnO to show the effect of geometry and materials. The Nyquist plot of the equivalent circuit (Supplementary Figs. 10 and 11 and Fig. 3b) demonstrates a lower resistance for QolorEX followed by flat ZnO/Al and flat ZnO. The semicircle part of the plot at high frequencies corresponds to electron-transfer-limited processes, and the linear part at low frequencies corresponds to diffusion processes<sup>27</sup>. Under illumination, the QolorEX plasmonic substrate has low charge transfer resistance ( $R_{CT}$ ), leading to a higher apparent electron transfer rate constant ( $k_{app}$ ) and fast redox kinetics (Fig. 3c). The lower resistance in the QolorEX surface under illumination can be correlated to the hot electron injection process<sup>20,28,29</sup>.

Next, we employed electrochemical impedance spectroscopy for characterization of QolorEX RT-LAMP amplification assays in the presence/absence of the target nucleic acid (Fig. 3d). We observed the enhanced reaction kinetics only in the presence of the target nucleic acid, which demonstrates that the hot electron injection under illumination directly affects the amplification and does not involve the side reactions, like phenol red oxidation (Supplementary Figs. 12 and 13). Here, QolorEX showed lower surface resistance under illumination compared to the dark state, resulting in high amplification reaction kinetics directly proportional to the target concentration (Fig. 3e). In the presence of plasmonic oscillation under ambient light illumination, the calculated electron transfer rate constant ( $k_{app}$ ) value for nucleic acid amplification in 130 nL media (the sensing chamber volume) was enhanced on average 9.15 times depending on the nucleic acid

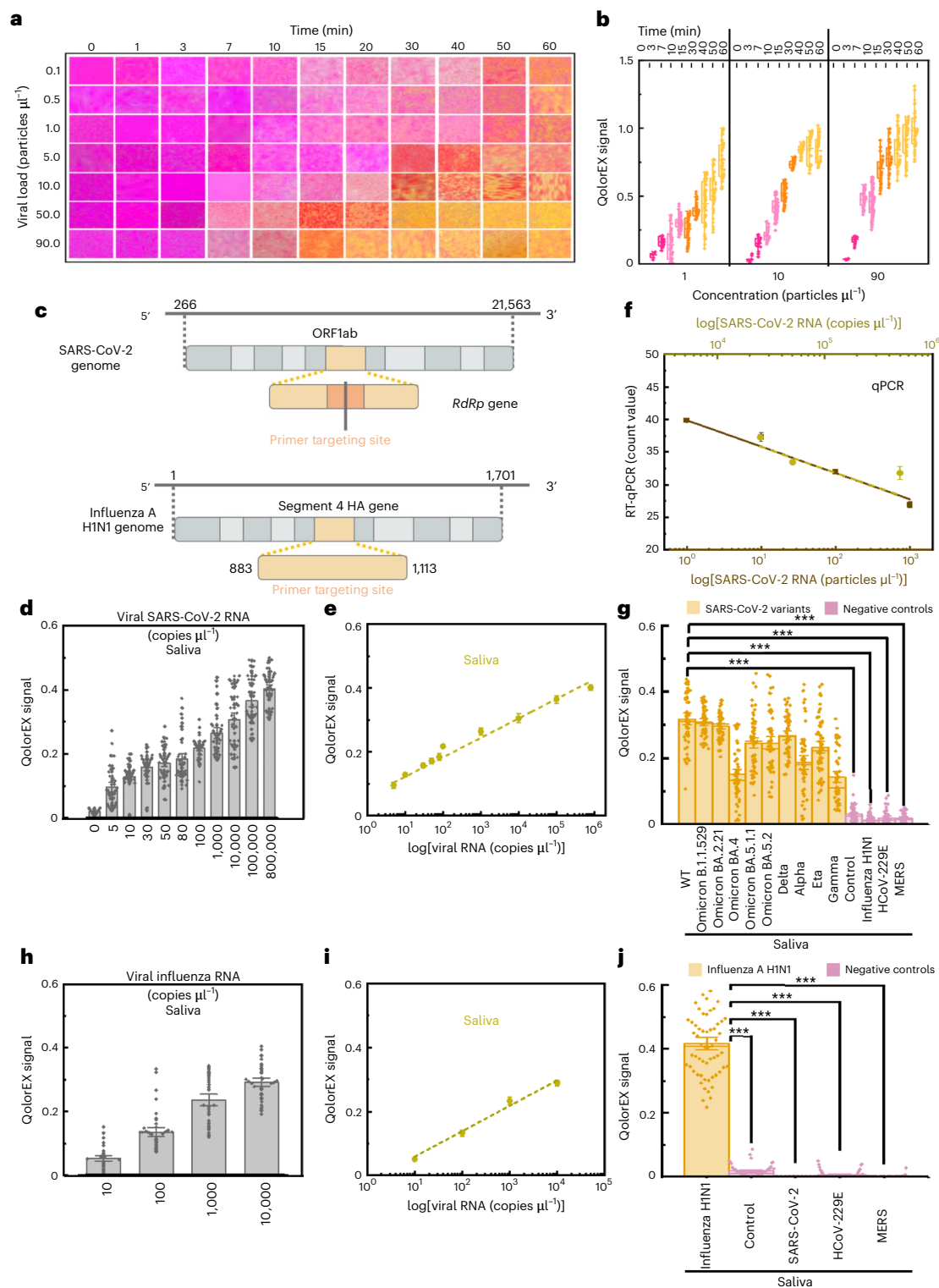


**Fig. 4 | QolorEX RT-LAMP analytical assay assessment in human saliva.**

**a**, Plasmonic enhanced colorimetric detection of SARS-CoV-2 viral samples in saliva. The colour palette represents the detected colorimetric read-out for different concentrations of SARS-CoV-2 (y-axis) versus time (x-axis). SARS-CoV-2 detection is shown by the rapid colour change from fuchsia to pink and then orange/yellow. **b**, The QolorEX signal read-out versus time for different viral loads. **c**, SARS-CoV-2 ORF1ab and H1N1 IAV segment 4 HA genomic maps indicating the target sequences used for this study. **d**, The magnitude of the QolorEX signal for different concentrations of SARS-CoV-2 RNA in saliva ( $N = 40$  per sample condition). **e**, The correlated linear relation of the QolorEX signal as a function of SARS-CoV-2 RNA concentration in saliva ( $R^2_{\text{SARS-CoV-2 RNA saliva}} = 0.97$ ). **f**, Standard reverse transcription qPCR calibration curve for SARS-CoV-2 heat-inactivated viral

particles (brown) and RNA (green). **g**, Selective quantification of the SARS-CoV-2 variants (WT, B.1.1.529, BA.4, BA.2.21, BA.5.2, BA.5.1.1, B.1.617.2, B.1.1.7, B.1.525 and P.1) versus multiple viral RNA and negative controls in saliva ( $N = 60$  per sample condition,  $F_{\text{SARS-CoV-2 RNA saliva}} = 97.75$ ,  $F_{\text{SARS-CoV-2 RNA saliva prob}} = 9.66822 \times 10^{-150}$ ). **h**, The magnitude of the QolorEX signal for different concentrations of H1N1 IAV RNA in saliva ( $N = 40$  per sample condition). **i**, The linear relation of the QolorEX signal as a function of H1N1 IAV RNA concentration in saliva ( $R^2_{\text{H1N1 RNA saliva}} = 0.99$ ). **j**, Quantification of the H1N1 IAV RNA selective detection versus different viral RNA and negative controls in saliva ( $N = 60$  per sample condition,  $F_{\text{H1N1 RNA saliva}} = 809.38036$ ,  $F_{\text{H1N1 RNA saliva prob}} = 1.74759 \times 10^{-152}$ ). Quantification of the data shows mean values  $\pm$  standard error of the mean with a coefficient of 1.5 for all panels. \*\*\* $P < 0.001$  as determined by one-way ANOVA with post hoc Tukey's test.



concentration (Fig. 3f). The excess electron flux in the oxidation step of the amplification reaction was further validated via cyclic voltammetry in the absence/presence of the light. Here, the oxidation peak amplification is higher when illuminated in the presence of the target, which supports our hypothesis of electron involvement in the amplification process. This experiment was repeated in different body fluids with a higher viscosity than buffer, which represented more resistance to the electron transfer<sup>8,30</sup>, resulting in lower oxidation current amplification peaks in saliva and nasopharyngeal fluid (Supplementary Fig. 12).

### QolorEX with LAMP for universal RNA/DNA detection

We illustrate the diagnostic capability of QolorEX coupled with RT-LAMP using a paradigm of viral respiratory infections such as severe acute respiratory syndrome coronavirus 2 (SARS-CoV-2) and influenza A virus (IAV) in human saliva and buffer (Supplementary Fig. 17). First, we establish the sensitivity with a series of dilutions of wild-type (WT) SARS-CoV-2 viral particles (0.01 to 90 viral particles per microlitre) in saliva and buffer. The sequential images of the colour-sensing chamber over a 60 min time lapse create a mosaic colour matrix (Fig. 4a and Supplementary Figs. 14 and 15) that shows a gradual colour change from fuchsia to yellow. A positive detection signal shows a consistent increase over time, where higher signals are associated with higher viral loads (Fig. 4b). The gene target (Fig. 4c) is in the SARS-CoV-2 open reading frame 1ab (ORF1ab) as per the recommendations of the World Health Organization (WHO)<sup>31</sup>. We used highly selective SARS-CoV-2 RT-LAMP primers (Supplementary Fig. 16a) targeting the RNA-dependant RNA polymerase (*RdRp*) gene<sup>32</sup>.

The QolorEX differentiable colorimetric signal has a positive linear correlation with heat-inactivated SARS-CoV-2 particles within the physiologically relevant range<sup>33</sup> of 0.01 to 90 viral particles per microlitre (Supplementary Fig. 17a,b). Similarly, the signal has a direct correlation with the concentration of the viral RNA within the physiological range of  $5$  to  $8 \times 10^5$  RNA copies per microlitre (ref. 33) in human saliva (Fig. 4d). Furthermore, saliva samples spiked with SARS-CoV-2 RNA have a linear signal trend with the concentration as shown in Fig. 4e. The serial dilutions of SARS-CoV-2 samples (viral particles and viral RNA) were also correlated with a qPCR assay (Fig. 4f) as a gold standard reference. The limit of detection (LOD) of QolorEX (five RNA copies per microlitre in saliva (Supplementary Table 2)) lies sufficiently below the requirements of the WHO for point-of-care tests<sup>34</sup>, on par with US Food and Drug Administration (FDA)-approved technologies and the literature (Supplementary Tables 3 and 4).

To establish the selectivity of QolorEX, we compared the positive signal of different SARS-CoV-2 variants in human saliva with that of interfering viral infections, including H1N1 IAV, human coronavirus 229E (HCoV-229E) and Middle East respiratory syndrome coronavirus (MERS-CoV). Through a null comparison of the selectivity (Fig. 4g), we observed a significant difference between the SARS-CoV-2 signal and the signal from other viruses ( $P < 0.001$ ). In addition, the detection of

SARS-CoV-2 in different biological fluids, including urine and serum (Supplementary Figs. 18 and 19), demonstrated the versatility of the approach.

To further investigate the universal application of QolorEX, we incorporated a highly selective RT-LAMP primer set (Supplementary Fig. 16b) for detection of H1N1 IAV RNA (NY/01/09 strain; Fig. 4c). The device generated a quantifiable colorimetric signal with a linear range of  $5$  to  $8 \times 10^5$  RNA copies per microlitre (Fig. 4h,i) and a LOD of four RNA copies per microlitre in human saliva (Supplementary Table 2). It also demonstrated a significant signal difference when tested against SARS-CoV-2, HCoV-229E and MERS-CoV ( $P < 0.001$ ; Fig. 4j).

In addition to respiratory viruses and as a proof of concept for DNA amplification, we demonstrated successful detection of *Escherichia coli* and methicillin-resistant *Staphylococcus aureus* (MRSA) in a wide linear range of  $7.2$  to  $7.2 \times 10^6$  genomic DNA (gDNA) copies per millilitre and  $1$  to  $10^5$  gDNA copies per millilitre, respectively (Supplementary Fig. 20). QolorEX also achieved a LOD of  $14.6$  gDNA copies per millilitre and  $11$  gDNA copies per millilitre for *E. coli* and MRSA, respectively (Supplementary Table 2).

### QolorEX with RCA for viral variant identification

The versatility of QolorEX can be extended to gene variants and subtypes at the level of SNP when coupled with an RCA-based padlock probe (PLP) assay using HiFi Taq DNA Ligase<sup>35</sup>. Here, we demonstrated differentiation between WT SARS-CoV-2, the Delta variant (B.1.617.2) and the Omicron variant (B.1.1.529) in buffer (Supplementary Fig. 22) and human saliva (Fig. 5) within a linear range of  $5$  to  $8 \times 10^5$  complementary DNA (cDNA) copies per microlitre. The RCA colorimetric read-out for SARS-CoV-2 cDNA shows a gradual colour change during the incubation time (Fig. 5a). Positive detection signals show a consistent increase over time (Fig. 5b), with higher cDNA concentrations associated with higher signals.

For RCA-based WT SARS-CoV-2 identification (QolorEX<sub>RCA-WT</sub>) by targeting the *RdRp* gene in ORF1ab (Fig. 5c), we demonstrated a quantifiable colorimetric signal in human saliva (Fig. 5d) with a well-defined linear correlation (Fig. 5e) and a LOD of  $6.2$  cDNA copies per microlitre in saliva (Supplementary Table 2). Moreover, QolorEX<sub>RCA-WT</sub> has shown selective detection of WT SARS-CoV-2 when challenged against Delta and Omicron variant cDNA (Fig. 5f), demonstrating a significant difference between the WT SARS-CoV-2 signal and other variants ( $P < 0.001$ ). For the SARS-CoV-2 Delta variant (QolorEX<sub>RCA-Delta</sub>), we targeted the L452R mutation (Fig. 5c), which is a non-synonymous spike protein mutation resulting from T22917G SNP and is linked with high transmissibility<sup>36</sup>. QolorEX<sub>RCA-Delta</sub> showed an increasing linear trend with cDNA concentration (Fig. 5g,h) in human saliva with a LOD of  $7.3$  cDNA copies per microlitre (Supplementary Table 2) and maintained selective detection towards Delta variant cDNA with a statistically significant signal difference in comparison to Omicron and WT cDNA (Fig. 5i). QolorEX<sub>RCA-Omicron</sub> targeted the P681H mutation (Fig. 5c), which is a non-synonymous mutation

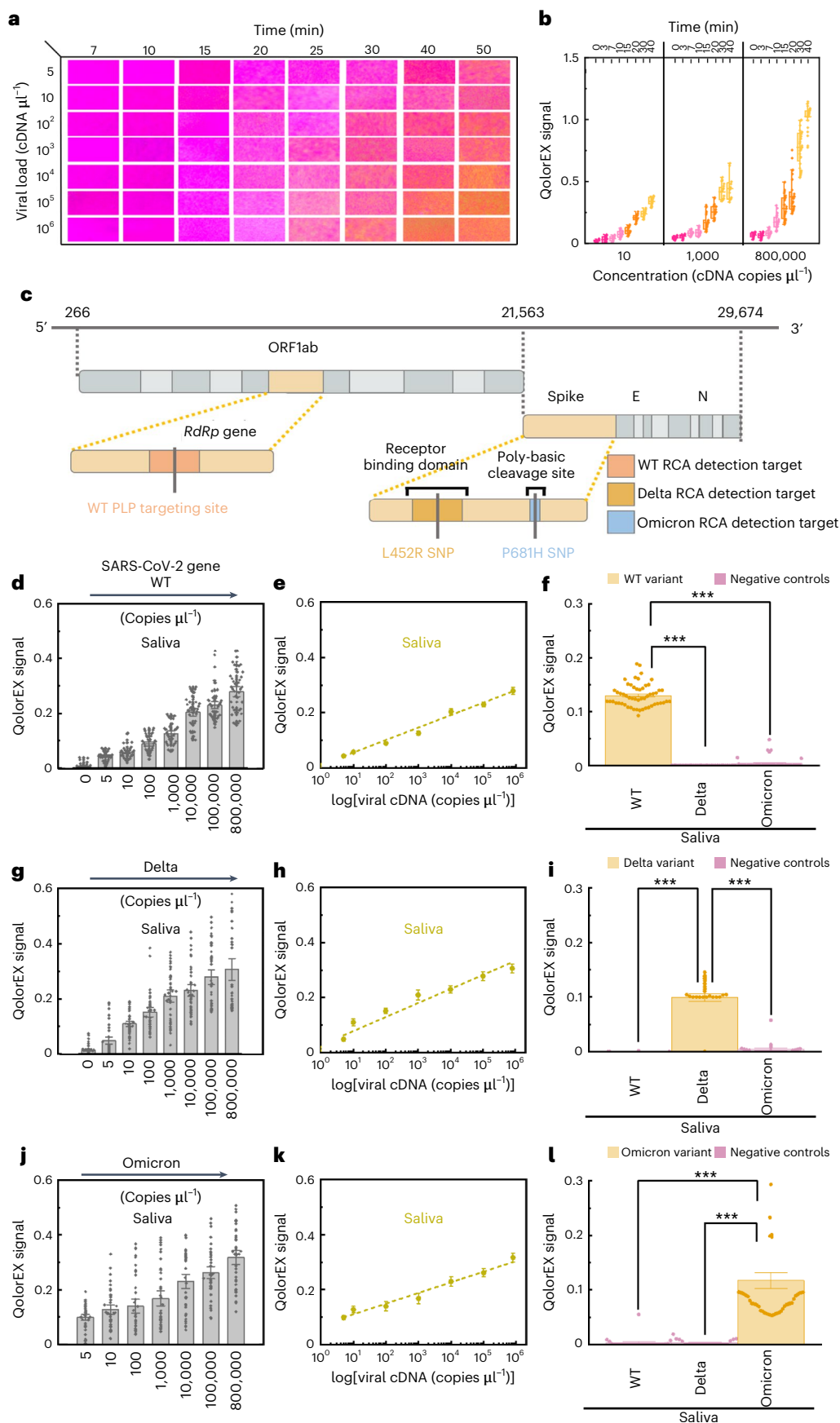
### Fig. 5 | QolorEX RCA analytical sensitivity and selectivity in human saliva.

**a**, Plasmonic enhanced colorimetric detection of SARS-CoV-2 variants of concern. The colour palette represents the detected colorimetric read-out for different concentrations of SARS-CoV-2 cDNA (y axis) versus time (x axis). SARS-CoV-2 detection is shown by the rapid colour change from fuchsia to pink and then orange/yellow. **b**, The corresponding QolorEX signal shows an overall increase in QolorEX signal output over time. **c**, SARS-CoV-2 genomic map indicating the target sequences used for this study. E, envelope gene; N, nucleocapsid gene. **d**, The magnitude of QolorEX<sub>RCA-WT</sub> signal for different concentrations of SARS-CoV-2 WT cDNA in saliva ( $N = 40$  per sample condition). **e**, The QolorEX<sub>RCA-WT</sub> signal as a linear function of SARS-CoV-2 WT cDNA concentration in saliva ( $R^2_{\text{saliva}} = 0.99$ ). **f**, Quantification of the QolorEX<sub>RCA-WT</sub> selective detection of the SARS-CoV-2 WT cDNA versus the cDNA of different SARS-CoV-2 variants in saliva ( $N = 60$ ,  $F_{\text{value}} = 2,005.41485$ ,  $F_{\text{prob}} = 2.50961 \times 10^{-122}$ ). **g**, The magnitude of the QolorEX<sub>RCA-Delta</sub> signal for different concentrations of

SARS-CoV-2 Delta variant cDNA in saliva ( $N = 40$  per sample condition). **h**, The QolorEX<sub>RCA-Delta</sub> signal as a linear function of SARS-CoV-2 Delta variant cDNA concentration in saliva ( $R^2_{\text{saliva}} = 0.96$ ). **i**, Quantification of the QolorEX<sub>RCA-Delta</sub> selective detection of the SARS-CoV-2 Delta variant cDNA versus the cDNA of different SARS-CoV-2 variants in saliva ( $N = 60$ ,  $F_{\text{value}} = 107.98492$ ,  $F_{\text{prob}} = 2.2123 \times 10^{-31}$ ). **j**, The magnitude of the QolorEX<sub>RCA-Omicron</sub> signal for different concentrations of SARS-CoV-2 Omicron variant cDNA in saliva ( $N = 40$  per sample condition). **k**, The QolorEX<sub>RCA-Omicron</sub> signal as a linear function of SARS-CoV-2 Omicron variant cDNA concentration in saliva ( $R^2_{\text{saliva}} = 0.97$ ). **l**, Quantification of the QolorEX<sub>RCA-Omicron</sub> selective detection of the SARS-CoV-2 Omicron variant cDNA versus the cDNA of different SARS-CoV-2 variants in saliva ( $N = 60$ ,  $F_{\text{value}} = 193.02268$ ,  $F_{\text{prob}} = 3.33077 \times 10^{-45}$ ). Quantification of the data shows mean values  $\pm$  standard error of the mean with a coefficient of 1.5 for all panels. \*\*\* $P < 0.001$  as determined by one-way ANOVA with post hoc Tukey's test.

caused by C23604A SNP and is associated with increased furin cleavage and higher infectivity<sup>36,37</sup>. QolorEX<sub>RCA-Omicron</sub> maintained a quantifiable linear correlation with target cDNA in saliva (Fig. 5j,k) with a LOD of

5.3 cDNA copies per microlitre (Supplementary Table 2) and maintained selectivity towards Omicron cDNA with a statistically significant signal difference in comparison to Delta and WT SARS-CoV-2 cDNA (Fig. 5l).





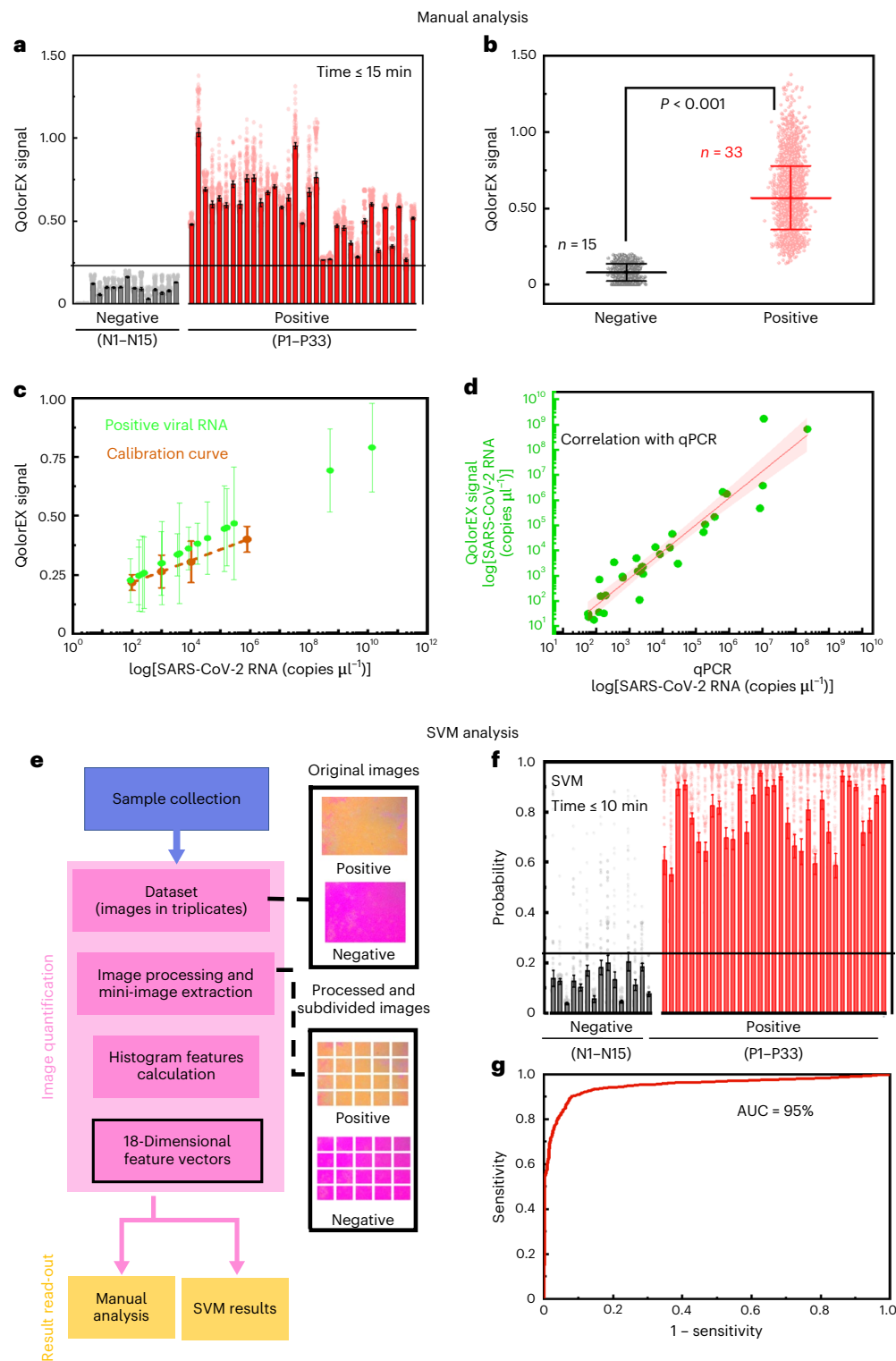


**Fig. 6 | Real-time monitoring of respiratory viral infection in uninfected and infected human samples.** **a**, QolorEX signal analysis comparing SARS-CoV-2-infected human samples (P1 to P33) to uninfected human samples (N1 to N15). Quantification of the data shows mean values  $\pm$  standard error of the mean with a coefficient of 1.5. **b**, Statistical analysis of the average QolorEX signal shows a clearly distinguished signal in SARS-CoV-2-infected human samples compared to uninfected human samples ( $P < 0.001$ ). The plot shows a data distribution with a total size of 90 for each uninfected and infected sample, the mean range and the s.d. with a coefficient of 1.0 ( $F$  value = 7,177.8141). **c**, Quantitative correlation of QolorEX colorimetric signal from human patient samples with the assay calibration curve for SARS-CoV-2 viral RNA load. The error bars show the s.d. with a coefficient of 1.0. **d**, Linear regression and 95% confidence interval of the

QolorEX quantitative response compared with qPCR. **e**, Flow chart of image quantification (with examples for negative and positive samples) and sample analysis (manual and machine learning). **f**, Comparison of the probability of SARS-CoV-2 infection obtained through a machine learning SVM model based on QolorEX signal between infected and uninfected human samples at 10 min. A probability threshold of 0.21 is established based on the comparison for the detection of SARS-CoV-2-positive samples with an  $F$  value of 549.77794 (quantification of the data shows mean values  $\pm$  standard error of the mean with a coefficient of 1.5). **g**, The receiver operating characteristic curve shows a  $0.95 \pm 0.00288$  AUC.  $N = 90$  per human sample, pertaining to ten colorimetry read-outs for each of the nine samplings.

## QolorEX validation with patient samples

We established QolorEX in a clinical setting with a set of 33 unprocessed COVID-19 patient samples and 15 SARS-CoV-2-negative human samples (Fig. 6a and Supplementary Fig. 23). A post hoc Tukey's test revealed a statistically significant signal contrast ( $P < 0.001$ ) between positive and negative samples (Fig. 6b). The signal from positive samples was compared with the established QolorEX calibration curve in Fig. 4e to estimate the viral load distribution (Fig. 6c), suggesting a high correlation with the tested linear range. The estimated viral load in comparison to the standard qPCR test (Supplementary Table 5) was highly correlated for positive samples (Fig. 6d), with median viral load values of  $3.6 \times 10^5$  and  $2.2 \times 10^5$  RNA copies per microlitre for qPCR and QolorEX tests respectively. Subsequently, we used a machine learning algorithm to classify the clinical samples into two classes: uninfected (negative) and infected (positive). A set of 90 mini-images per time point was used for the analysis of each sample (Fig. 6e). To evaluate the detection time, the first five incubation time points were analysed via a supervised binary support vector machine (SVM) algorithm (Supplementary Fig. 14). We implemented the optimum detection time of 10 min (Supplementary Fig. 14c) to obtain the probability of SARS-CoV-2 infection. This resulted in a 75% reduction in detection time compared to the original RT-LAMP assay<sup>32</sup>. We investigated the average probability of each clinical sample for being SARS-CoV-2-positive (Fig. 6f) and established a threshold of 0.21 as the cut-off value to differentiate between negative and positive samples. The cumulative true positive and true negative of patient samples are 100%. The receiver operating characteristic curve (Fig. 6g) of the classification of positive and negative samples shows an area under the curve (AUC) of 0.95 per test, demonstrating the satisfactory performance of the SVM algorithm connected to the QolorEX system.

## Conclusions

QolorEX combines rapidity, clinically relevant sensitivity, specificity and versatility for the detection of a variety of pathogens (viruses and bacteria) in an automated multiplex platform that is deployable at the point of care in low-resource, remote or congregate settings.

The first key feature of QolorEX is the integratable fabless self-assembly plasmonic nanostructures in a confined microfluidic device, resulting in hot electron injection from the surface of the nano-plasmonic sensor into the nanolitre volume of media upon illumination with ambient light—a mechanistic phenomenon. The plasmonic hot-spot catalysis in this system results in a ninefold acceleration of the amplification kinetics and thus provides the fastest colorimetric signal transduction (less than 10 min) reported to date<sup>8,10,38</sup>. It also enhances the sensitivity of the one-step amplification via RT-LAMP and RCA, allowing the detection of a few copies of genomic RNA/DNA at the level of SNP. The second feature of QolorEX is a microfluidic cartridge that offers precise spatial and temporal control over fluidic volumes via mechanically driven submillimetre-sized thin elastomeric chambers, eliminating other passive techniques with required complex design strategies<sup>39,40</sup> and/or the use of bulky/expensive active fluid manipulation techniques<sup>41,42</sup>. This microfluidic cartridge enables the automation of sequential steps of a typical amplification assay, including on-chip lysis, extraction, reagents mixing and detection—a step forward towards the point-of-care functionality of QolorEX in comparison with recent technologies that perform reagent preparation off-chip<sup>43,44</sup>.

QolorEX presents an automated and user-friendly set-up for multiplexed testing with a turnaround time of 13 min (3 min lysis and 10 min detection) and minimal intervention from users. With a two-step operation, the operator simply introduces their saliva into a microfluidic cartridge and places it in a fully automated apparatus that incorporates a supervised machine learning algorithm to interpret and communicate the results via cell phone. By testing different respiratory viruses (SARS-CoV-2, H1N1 IAV) and bacteria

(*E. coli*, MRSA), we demonstrated the versatility of QolorEX for the specific detection of different pathogens as well as differentiation at the level of SNP between different target variants and subvariants of SARS-CoV-2. Further, QolorEX has been successfully established in a clinical setting by validation with unprocessed samples obtained from 33 infected individuals clinically diagnosed with SARS-CoV-2 against 15 samples from uninfected individuals. Additionally, QolorEX achieved a clinically relevant sensitivity and specificity with 95% accuracy on par with qPCR as required by WHO's framework for point-of-care tests<sup>34</sup>.

Overall, the accuracy of QolorEX in saliva is notable for its rapidity and automation compared with previous RNA/DNA testing technologies<sup>2,45–49</sup>. We believe that QolorEX is an important step forward in developing point-of-care diagnostics in support of rapid intervention against infectious diseases and monitoring emerging infections and variants. QolorEX and its cell phone interface can help with large-scale harmonized data collection, rapid situation evaluation and decision-making. Further, we believe that the potential of QolorEX can expand into other health care applications (including but not limited to real-time diagnostics and drug efficacy testing).

## Online content

Any methods, additional references, Nature Portfolio reporting summaries, source data, extended data, supplementary information, acknowledgements, peer review information; details of author contributions and competing interests; and statements of data and code availability are available at <https://doi.org/10.1038/s41565-023-01384-5>.

## References

- Peeling, R. W., Heymann, D. L., Teo, Y. Y. & Garcia, P. J. Diagnostics for COVID-19: moving from pandemic response to control. *Lancet* **399**, 757–768 (2022).
- MicroGem. *MicroGEM Sal6830SARS-CoV-2 Saliva Test Instructions for Use (IFU)* <https://www.fda.gov/media/157754/download> (2022).
- DxLab. *DxLab COVID-19 Test Instructions For Use (IFU)* <https://www.fda.gov/media/158980/download> (2022).
- Will, S. Companies are racing to develop COVID-19 tests for the US. Will tests help? *C&EN Glob. Enterp.* **98**, 30–32 (2020).
- Mahshid, S. S., Flynn, S. E. & Mahshid, S. The potential application of electrochemical biosensors in the COVID-19 pandemic: a perspective on the rapid diagnostics of SARS-CoV-2. *Biosens. Bioelectron.* **176**, 112905 (2021).
- Mats, N. et al. Padlock probes: circularizing oligonucleotides for localized DNA detection. *Science* **265**, 2085–2088 (1994).
- Hardenbol, P. et al. Multiplexed genotyping with sequence-tagged molecular inversion probes. *Nat. Biotechnol.* **21**, 673–678 (2003).
- Dao Thi, V. L. et al. A colorimetric RT-LAMP assay and LAMP-sequencing for detecting SARS-CoV-2 RNA in clinical samples. *Sci. Transl. Med.* **12**, eabc7075 (2020).
- Wang, C. et al. Point-of-care diagnostics for infectious diseases: from methods to devices. *Nano Today* **37**, 101092 (2021).
- Alafeef, M., Moitra, P., Dighe, K. & Pan, D. RNA-extraction-free nano-amplified colorimetric test for point-of-care clinical diagnosis of COVID-19. *Nat. Protoc.* **16**, 3141–3162 (2021).
- Lin, H. et al. Ferrobotic swarms enable accessible and adaptable automated viral testing. *Nature* **611**, 570–577 (2022).
- Hu, M. et al. Gold nanostructures: engineering their plasmonic properties for biomedical applications. *Chem. Soc. Rev.* **35**, 1084–1094 (2006).
- Tao, A., Sinsermsuksakul, P. & Yang, P. Tunable plasmonic lattices of silver nanocrystals. *Nat. Nanotechnol.* **2**, 435–440 (2007).
- Knight, M. W. et al. Aluminum for plasmonics. *ACS Nano* **8**, 834–840 (2014).

15. Liu, T. et al. Quantification of antibody avidities and accurate detection of SARS-CoV-2 antibodies in serum and saliva on plasmonic substrates. *Nat. Biomed. Eng.* **4**, 1188–1196 (2020).
16. Liu, Y. et al. Digital plasmonic nanobubble detection for rapid and ultrasensitive virus diagnostics. *Nat. Commun.* **13**, 1687 (2022).
17. Liu, J. G., Zhang, H., Link, S. & Nordlander, P. Relaxation of plasmon-induced hot carriers. *ACS Photon.* **5**, 2584–2595 (2018).
18. Brongersma, M. L., Halas, N. J. & Nordlander, P. Plasmon-induced hot carrier science and technology. *Nat. Nanotechnol.* **10**, 25–34 (2015).
19. Kim, Y., Wilson, A. J. & Jain, P. K. The nature of plasmonically assisted hot-electron transfer in a donor–bridge–acceptor complex. *ACS Catal.* **7**, 4360–4365 (2017).
20. Zilio, P., Dipalo, M., Tantussi, F., Messina, G. C. & De Angelis, F. Hot electrons in water: injection and ponderomotive acceleration by means of plasmonic nanoelectrodes. *Light. Sci. Appl.* **6**, e17002 (2017).
21. Rao, V. G., Aslam, U. & Linic, S. Chemical requirement for extracting energetic charge carriers from plasmonic metal nanoparticles to perform electron-transfer reactions. *J. Am. Chem. Soc.* **141**, 643–647 (2019).
22. Cortés, E. et al. Challenges in plasmonic catalysis. *ACS Nano* **14**, 16202–16219 (2020).
23. Chen, Y.-C. et al. Au@Nb@H<sub>x</sub>K<sub>1-x</sub>NbO<sub>3</sub> nanopeapods with near-infrared active plasmonic hot-electron injection for water splitting. *Nat. Commun.* **9**, 232 (2018).
24. Zhang, P., Wang, T. & Gong, J. Mechanistic understanding of the plasmonic enhancement for solar water splitting. *Adv. Mater.* **27**, 5328–5342 (2015).
25. Kottur, J. & Nair, D. T. Pyrophosphate hydrolysis is an intrinsic and critical step of the DNA synthesis reaction. *Nucleic Acids Res.* **46**, 5875–5885 (2018).
26. Corson, E. R., Creel, E. B., Kostecki, R., McCloskey, B. D. & Urban, J. J. Important considerations in plasmon-enhanced electrochemical conversion at voltage-biased electrodes. *iScience* **23**, 100911 (2020).
27. Siavash Moakhar, R. et al. A versatile biomimic nanotemplating fluidic assay for multiplex quantitative monitoring of viral respiratory infections and immune responses in saliva and blood. *Adv. Sci.* **9**, e2204246 (2022).
28. Wang, P., Krasavin, A. V., Nasir, M. E., Dickson, W. & Zayats, A. V. Reactive tunnel junctions in electrically driven plasmonic nanorod metamaterials. *Nat. Nanotechnol.* **13**, 159–164 (2018).
29. Dombi, P. et al. Ultrafast strong-field photoemission from plasmonic nanoparticles. *Nano Lett.* **13**, 674–678 (2013).
30. Torres, M. D. T., de Araujo, W. R., de Lima, L. F., Ferreira, A. L. & de la Fuente-Nunez, C. Low-cost biosensor for rapid detection of SARS-CoV-2 at the point of care. *Matter* **4**, 2403–2416 (2021).
31. Corman, V. et al. Diagnostic Detection of Wuhan Coronavirus 2019 by Real-Time RT-PCR <https://www.who.int/docs/default-source/coronaviruse/wuhan-virus-assay-v1991527e5122341d99287a1b17c111902.pdf> (World Health Organization, 2020).
32. Yu, L. et al. Rapid detection of COVID-19 coronavirus using a reverse transcriptional loop-mediated isothermal amplification (RT-LAMP) diagnostic platform. *Clin. Chem.* **66**, 975–977 (2020).
33. Lin, Y.-C. et al. Detection and quantification of infectious severe acute respiratory coronavirus-2 in diverse clinical and environmental samples. *Sci. Rep.* **12**, 5418 (2022).
34. Cubas-Atienzar, A. I. et al. Limit of detection in different matrices of 19 commercially available rapid antigen tests for the detection of SARS-CoV-2. *Sci. Rep.* **11**, 18313 (2021).
35. New England Biolabs. HiFi Taq DNA Ligase <https://international.neb.com/products/m0647-hi-fi-taq-dna-ligase> (2021).
36. Glue: SARS-COV-2 mutations. CoV Available at: <https://cov-glue.cvr.gla.ac.uk/> (CVR, 2021).
37. Liping, Z. et al. Furin cleavage of the SARS-CoV-2 spike is modulated by O-glycosylation. *Proc. Natl Acad. Sci. USA* **118**, e2109905118 (2021).
38. Zhang, T. et al. A paper-based assay for the colorimetric detection of SARS-CoV-2 variants at single-nucleotide resolution. *Nat. Biomed. Eng.* **6**, 957–967 (2022).
39. Yafia, M. et al. Microfluidic chain reaction of structurally programmed capillary flow events. *Nature* **605**, 464–469 (2022).
40. Narayanamurthy, V. et al. Advances in passively driven microfluidics and lab-on-chip devices: a comprehensive literature review and patent analysis. *RSC Adv.* **10**, 11652–11680 (2020).
41. Najjar, D. et al. A lab-on-a-chip for the concurrent electrochemical detection of SARS-CoV-2 RNA and anti-SARS-CoV-2 antibodies in saliva and plasma. *Nat. Biomed. Eng.* **6**, 968–978 (2022).
42. Lee, W.-B. et al. A microfluidic device for antimicrobial susceptibility testing based on a broth dilution method. *Biosens. Bioelectron.* **87**, 669–678 (2017).
43. Jagannath, A. et al. Pathogen detection on microfluidic platforms: recent advances, challenges, and prospects. *Biosens. Bioelectron. X* **10**, 100134 (2022).
44. Nguyen, T. et al. Point-of-care devices for pathogen detections: the three most important factors to realise towards commercialization. *TrAC Trends Anal. Chem.* **131**, 116004 (2020).
45. Cue Health. The Cue™ COVID-19 Test for Home and Over The Counter (OTC) Use Instructions For Use <https://www.fda.gov/media/146470/download> (2022).
46. Ceci, A. et al. Development and implementation of a scalable and versatile test for COVID-19 diagnostics in rural communities. *Nat. Commun.* **12**, 4400 (2021).
47. Arizti-Sanz, J. et al. Simplified Cas13-based assays for the fast identification of SARS-CoV-2 and its variants. *Nat. Biomed. Eng.* **6**, 932–943 (2022).
48. Welch, N. L. et al. Multiplexed CRISPR-based microfluidic platform for clinical testing of respiratory viruses and identification of SARS-CoV-2 variants. *Nat. Med.* **28**, 1083–1094 (2022).
49. de Helena, P. et al. Minimally instrumented SHERLOCK (miSHERLOCK) for CRISPR-based point-of-care diagnosis of SARS-CoV-2 and emerging variants. *Sci. Adv.* **7**, eabh2944 (2022).

**Publisher's note** Springer Nature remains neutral with regard to jurisdictional claims in published maps and institutional affiliations.

Springer Nature or its licensor (e.g. a society or other partner) holds exclusive rights to this article under a publishing agreement with the author(s) or other rightsholder(s); author self-archiving of the accepted manuscript version of this article is solely governed by the terms of such publishing agreement and applicable law.

© The Author(s), under exclusive licence to Springer Nature Limited 2023



## Methods

### Study design

This study was approved by the McGill Research Ethics Office (Institutional Review Board, A03-M24-21B). It was intended to develop a universal platform for the molecular detection of respiratory tract infections at the point of care. We used H1N1 influenza A, SARS-CoV-2 RNA and SARS-CoV-2 heat-inactivated viral particles for rapid diagnostics based on plasmonically enhanced RT-LAMP assays. MERS-CoV RNA and HCoV-229E RNA were used as negative controls for the RT-LAMP assays. Moreover, an RCA assay was used for the specific detection of SARS-CoV-2 variants of concern. Last, we used 33 deidentified SARS-CoV-2-positive human samples (RT-PCR verified) obtained from University Health Network's PRESERVE Pandemic Response Biobank and 15 SARS-CoV-2-negative samples (qPCR verified) as controls in the patient sample study. As proof of principle, DNA profiling of *E. coli* and MRSA was carried out using LAMP assays. *Pseudomonas aeruginosa* was used as a negative control for the LAMP assays. This study was conducted in Montreal, Canada, from April 2020 to December 2022.

### Materials

Materials were sourced as follows: polystyrene nanobeads (polystyrene particles (PS-R); Micro Particle); synthetic SARS-CoV-2 RNA (American Type Culture Collection (ATCC); Cedarlane); SARS-CoV-2 B.1.1.7 Alpha variant RNA (ATCC VR-3326D; Cedarlane); MERS-CoV (ATCC VR-3248SD; Cedarlane); heat-inactivated SARS-CoV-2 (ATCC VR-1986HK; Cedarlane); heat-inactivated H1N1 influenza A, NY/01/09 strain (0810248CFHI; Cedarlane); and *E. coli* (no. 211540, Merlan Scientific). Colorimetric RT-LAMP master mix and HiFi Taq DNA Ligase enzyme (New England Biolabs); PLPs, RCA primers and synthetic cDNA SARS-CoV-2 targets, MgCl<sub>2</sub>, KCl, nicotinamide adenine dinucleotide (NAD) and Triton X-100 (Sigma Aldrich); and LAMP primers and dithiothreitol (DTT) (Thermo Fisher Scientific) were used. Healthy human pooled saliva (IRHUS-L50ML) and healthy human single-donor saliva (IRHUSLS5ML) were bought from Innovative Research and stored upon arrival at -80 °C. SARS-CoV-2 variant (Omicron, Delta, Eta and Gamma) RNA samples were obtained from the cooperator laboratory at McGill University (Vidal Lab). HCoV-229E RNA was obtained from the cooperator laboratory at Lady Davis Institute for Medical Research in Jewish General Hospital (C. Liang laboratory). MRSA DNA and *P. aeruginosa* DNA were obtained from the D. Nguyen laboratory at McGill University Health Centers (MUHC) research institute. All assays were prepared using UltraPure DNase/RNase-free distilled water (Thermo Fisher Scientific).

### Primers and probes

The SARS-CoV-2 RT-LAMP primers used in this study were designed by Yu et al.<sup>32</sup> to target the *RdRp* gene in the ORF1ab of the genome (recommended by the WHO as a target gene for SARS-CoV-2 detection)<sup>31</sup>. The primer selectivity was confirmed through a gel electrophoresis experiment (Supplementary Fig. 16a). The primers' compositions and concentrations are available in Supplementary Table 6.

H1N1 RT-LAMP primers were designed with the New England Biolabs LAMP Primer Design Tool targeting highly conserved sequences of the hemagglutinin (HA) gene of H1N1 IAV. The LAMP recognition part was evaluated by the Basic Local Alignment Search Tool<sup>50</sup>, and no sequence variations were seen in 100 hits provided by the National Center for Biotechnology Information website. The nominated LAMP primers were selected according to the optimized parameters offered by the Primer Explorer V5 protocol. The primers selectivity was further confirmed through a gel electrophoresis experiment (Supplementary Fig. 16b). The primers' compositions and concentrations are available in Supplementary Table 7.

The P681H and L452R mutation sites were determined according to the CoV-GLUE-Viz and GISAID tools<sup>36,51</sup>, and PLP recognition parts were designed to be specific to the mutations<sup>36</sup>. In addition, the PLP target site for WT SARS-CoV-2 detection was the *RdRp* gene, which is

the same as the targeting site for SARS-CoV-2 LAMP primers. The PLPs are designed in a way that the SNP is distinguished by the upstream of the PLP, which provides the 3'-hydroxyl group at the ligation junction base-paired next to the phosphorylated 5' end on a target strand. The veracity of PLP circularization upon SNP detection has been determined using the Thermostable Ligase Reaction Temperature Calculator provided by New England Biolabs. Thereafter, the PLPs were evaluated using the Mfold web server to avoid undesirable secondary structure, especially in the PLP recognition site. RCA forward and reverse primers were designed to be hybridized to the spacer part of PLPs that connects two specific arms of the PLP altogether. PLP selectivity was confirmed through a gel electrophoresis experiment (Supplementary Fig. 21). PLP compositions and concentrations, as well as RCA primer compositions and concentrations and cDNA composition, are available in Supplementary Tables 8–10.

The bacterial LAMP primers used in this study were designed by Hill et al.<sup>52</sup> for targeting the *E. coli* *malB* gene and Chen et al.<sup>53</sup> for targeting the MRSA *mecA* gene. Primers' compositions and concentrations are available in Supplementary Tables 11 and 12.

### Assay preparation

For RT-LAMP assays, a standard reaction volume of 20 µl was used. This volume consisted of 2 µl ×10 primer mix, 10 µl ×2 master mix, 7 µl RNase-free water and 1 µl RNA sample. Heat-inactivated viral samples were first thermally lysed at 95 °C for 3 min and then mixed with the assay. This was followed by incubation at 65 °C for different periods to visualize colour change versus time for different samples.

The PLP ligation reaction was performed in a final volume of 10 µl including 1 µl synthetic cDNA of SARS-CoV-2 RNA genome, 1 µl of 1 µM PLP, 2 µl UltraPure distilled water and 5 µl ×2 no-Tris-HCl HiFi Taq DNA Ligase ligation solution (20 mM MgCl<sub>2</sub>, 20 mM KCl, 2 mM NAD, 0.1% Triton X-100, 20 mM DTT, pH 8.50) and 1 µl HiFi Taq DNA Ligase enzyme. The ligation mixture was first incubated at 95 °C for 5 min for DNA denaturation and then cooled to PLP annealing temperatures (which are 60, 58 and 55 °C for P681H, L452R and WT PLPs, respectively) to let PLPs hybridize with cDNA and ligate via HiFi enzyme in a thermocycler (Analytik Jena). Thereafter, the ligation reaction used 12 µl of WarmStart Colorimetric LAMP ×2 Master Mix and 1.6 µM RCA reverse and forward primers in a final volume of 24 µl. The RCA amplification reaction was performed at 65 °C for different periods to visualize the colour change versus time for different samples.

For bacterial DNA extraction, *E. coli* samples were cultured overnight at 37 °C in Luria Broth media. Bacteria concentration was determined using a Spectronic 21D spectrophotometer. Aliquots of different concentrations of 10<sup>7</sup> CFU ml<sup>-1</sup>, 10<sup>5</sup> CFU ml<sup>-1</sup>, 10<sup>4</sup> CFU ml<sup>-1</sup>, 10<sup>3</sup> CFU ml<sup>-1</sup>, 10<sup>2</sup> CFU ml<sup>-1</sup> and 10 CFU ml<sup>-1</sup> were prepared by suspending *E. coli* cultures in Luria Broth media. *E. coli* DNA was extracted by boiling cultures at 95 °C for 10 min. MRSA DNA was obtained from the McGill University Health Centre using the chemical lysis method. All DNA sample concentrations were measured using a Nanodrop 2000 spectrophotometer and suspended in Universal Buffer 48 (Bio Basic) to achieve desired concentrations.

The QolorEX assay for SARS-CoV-2 tested spiked solutions (RNase-free water and healthy saliva) of 8 × 10<sup>5</sup> RNA copies µl<sup>-1</sup> to 5 RNA copies µl<sup>-1</sup> of SARS-CoV-2 RNA and 90 viral particles µl<sup>-1</sup> to 0.01 viral particles µl<sup>-1</sup> for heat-inactivated SARS-CoV-2 to fit in a biologically relevant range. Similarly, a study was performed for Delta B.1.617.2, Omicron B.1.1.529, Omicron BA.4, Omicron BA.2.21, Omicron BA.5.2, Omicron BA.5.1.1, Eta B.1.525 and Gamma P.1 with 8 × 10<sup>5</sup> RNA copies µl<sup>-1</sup> to 10<sup>4</sup> RNA copies µl<sup>-1</sup>.

The QolorEX assay for H1N1 studied spiked solutions (RNase-free water and healthy saliva) of 8 × 10<sup>5</sup> RNA copies µl<sup>-1</sup> to 5 RNA copies µl<sup>-1</sup> of H1N1 influenza A RNA. For selectivity studies, RNA from multiple viruses (SARS-CoV-2, MERS-CoV and HCoV-229E) was used at 8 × 10<sup>5</sup> RNA copies µl<sup>-1</sup>.



The QolorEX assay for *E. coli* studied spiked solutions (RNase-free water) of  $7.2 \times 10^6$  gDNA copies  $\text{ml}^{-1}$  to  $7.2$  gDNA copies  $\text{ml}^{-1}$ , equivalent to  $0.0343$  ng  $\mu\text{l}^{-1}$  to  $3.43 \times 10^{-8}$  ng  $\mu\text{l}^{-1}$  of *E. coli* DNA. For selectivity studies, DNA from multiple bacteria (*E. coli*, MRSA and *P. aeruginosa*) was tested at the concentration of  $10^2$  gDNA copies  $\mu\text{l}^{-1}$ .

The QolorEX assay for MRSA studied spiked solutions (RNase-free water) of  $10^5$  gDNA copies  $\text{ml}^{-1}$  to  $1$  gDNA copy  $\text{ml}^{-1}$ , equivalent to  $3.05 \times 10^{-4}$  ng  $\mu\text{l}^{-1}$  to  $3.05 \times 10^{-9}$  ng  $\mu\text{l}^{-1}$  of MRSA DNA. For selectivity studies, DNA from multiple bacteria (MRSA, *E. coli* and *P. aeruginosa*) was tested at the concentration of  $10^2$  gDNA copies  $\mu\text{l}^{-1}$ .

The QolorEX RCA assay was done in spiked solutions (RNase-free water and healthy saliva) of  $8 \times 10^5$  cDNA copies  $\mu\text{l}^{-1}$  to  $5$  cDNA copies  $\mu\text{l}^{-1}$  of synthetic cDNA of P681H, L452R and WT SARS-CoV-2 sequences. For selectivity, the P681H PLP was evaluated in the presence of P681H, WT-P681H and L452R cDNA. The same strategy was employed for the selectivity testing of L452R PLP using L452R, WT- L452R and P681H cDNA targets as well as WT PLP in the presence of WT, P681H and L452R cDNA sequences. All the cDNA targets were assessed at concentrations of  $10^5$  cDNA copies  $\mu\text{l}^{-1}$ .

### QolorEX automated sample handling and imaging box

The portable imaging set-up has three major components: the epi-illumination imaging set-up, fluid handling module and automation components (Supplementary Fig. 1). The outer enclosure of the set-up is completely fabricated by fused deposition modelling 3D printing (Prusa I3 Mk3, Prusa) at  $0.3$ -mm-layer resolution.

The epi-illumination imaging set-up was designed to capture the colorimetric change of the assay solution. The imaging set-up has an illumination module and an image capture and processing module. A  $\times 20$  objective (TU Plan Fluor EPI  $\times 20$ , Nikon) was used as the condenser lens for image capture. All the optical components employed were procured from Thorlabs. The final image is projected onto a CMOS sensor (Sony IMX477R, 12.3MP, Raspberry Pi.) and processed further by Raspberry Pi 4 (Raspberry Pi).

For process automation, we employed five linear actuators (Actuonix) that carry out multiple steps in fluid handling (Supplementary Figs. 1–3). The set-up employs a heater module, which is a portable solder iron (TS-100), for sample lysis. An XY translation stage was employed to scan different intra- and inter-regions of the detection chambers. We used a linearly guided computerized numerical control stage that is driven by a stepper motor (FUYU). Both the actuator system and the stage are controlled with an Arduino UNO microcontroller (Arduino). The two heating elements are controlled with a two-channel relay module (Yizhet). Automated transfer and analysis of data in our system are controlled by a Raspberry Pi 4 (Raspberry Pi) microcontroller. The results are displayed on an application designed by MIT App Inventor (Supplementary Fig. 2).

### Microfluidic cartridge and plasmonic platform fabrication

The fabrication process followed an established protocol<sup>27,54,55</sup> and is detailed in the Supplementary Information (Supplementary Fig. 5). Briefly, the microfluidic cartridge is based on a six-inch silicon wafer. A three-step lithography process is used to pattern the impeded heater element and the microfluidic features. First, a lithography step is carried out to transfer the heater (width,  $400$   $\mu\text{m}$ ) and pad (length,  $5$  mm; width,  $2$  mm) features to a photoresist layer through a photomask with the desired patterns. This is followed by a buffered oxide etch to remove the native oxide and a potassium hydroxide etch for a  $200$  nm silicon etch. Next, a lift-off process for selective deposition of the heater elements in the etched grooves is carried out. This starts with a second lithography step followed by an electron-beam deposition of  $240$  nm Al using the Temescal BJD 1800. Accordingly, the lift-off is completed by submersion in suitable remover. Next, the last lithography step is carried out to pattern the fluidic device features including inlet/outlet ports

(diameter  $2$  mm), lysis chamber (length,  $1.74$  mm; width,  $1.5$  mm; depth,  $50$   $\mu\text{m}$ ), mixing channels (width,  $200$   $\mu\text{m}$ ; height,  $50$   $\mu\text{m}$ ) and plasmonic window (length,  $1.94$  mm; width,  $1.5$  mm; height,  $50$   $\mu\text{m}$ ) into a SU-8 layer (SU-8 2050). Subsequently, the six-inch wafer is diced into individual chips (length,  $26.5$  mm; width,  $35$  mm) using a Disco DAD 3240 dicing saw.

This is followed by the integration of the colour-sensitive platforms in the microfluidic cartridge using a fabless nanopatterning technique. A generic approach is used to develop a colloidal self-assembly monolayer of nanoparticles at a water–air interface<sup>56</sup>. Next, the resulting honeycomb structures are transferred to the colour detection chamber in the microfluidic cartridge. Subsequently, a ZnO thin film ( $120$  nm) is deposited, followed by a thin Al layer ( $10$  nm) to provide a tunable localized surface plasmon resonance with a white background.

Polydimethylsiloxane (PDMS) is prepared using a 10:1 ratio of elastomer to crosslinker, degassed in a desiccator and incubated at  $65$  °C overnight. The cured PDMS is cut in the size of the microfluidic cartridge, and inlet/outlet ports are punched using a PDMS puncher (Thermo Fisher Scientific) and used to seal the devices. The sealing process includes a  $50$  second plasma treatment followed by overnight incubation at  $105$  °C. Next, a PDMS-based suction cup layer was fabricated using stereolithography (SLA) 3D-printed moulds (Form 3, Formlabs). The suction cups were subsequently bonded to the fluidic PDMS layer by plasma-activated bonding.

Sample processing cartridges (manufactured using an SLA 3D printer at  $50$   $\mu\text{m}$  resolution on the  $z$  axis) are bonded to the PDMS-covered microfluidic chip using a double-sided tape conducive to plasma-activated bonding and placed in an oven at  $95$  °C for  $90$  min. In the 3D-printed cartridge, there are two brass metal inserts (McMaster Carr) for sample lysis.

### Image processing

Image processing starts with a dataset composed of triplicate images from each condition studied, which will be divided into mini-images to generate a total of  $40$  and  $60$  data points per condition for sensitivity and selectivity, respectively. Specifically for the clinical samples, each was studied in three parallel collection chambers of the microfluidic chip; since all images are taken in triplicate and then divided, a total of  $90$  data points were studied for each patient sample. All the image processing consists of cropping the outer  $20\%$  of the original RGB image to remove the coffee ring effect<sup>57</sup>, followed by a blue filter application, where pixels with a hue value between  $85$  and  $140$  (blue range) are removed and replaced by the mean value of the rest of the image<sup>57</sup>. The blue-filtered image is then thresholded by replacing the  $25\%$  less saturated pixels with the mean value of the rest of the filtered image. Finally, the processed image is cut into sub-images from which several features are extracted, consequential to the implementation of formulas detailed in Sergyan<sup>58</sup>. The modification made to the formulas consists of interchanging the greyscale intensity with the intensity of each RGB channel<sup>58</sup>. A total of  $18$  values are extracted from each sub-image corresponding to the mean colour value, standard deviation, mode, skew, energy and entropy for each of the RGB channels.

For the automation of the real human samples, we implemented a supervised machine learning algorithm to classify the images into two classes, uninfected and infected (Supplementary Fig. 14). An SVM with a radial basis function (RBF) kernel was established with its hyperparameters  $C$  and  $\gamma$  assessed by a Bayesian search<sup>59</sup> and an overfitting absence validated via a fivefold cross-validation. The database for this study is integrated by  $33$  infected and  $15$  uninfected controls; for every sample, studies were conducted in triplicate, acquiring a total of nine images per time point. The datasets are divided into two classes: uninfected (negative) and infected (positive). Then they are divided into distinct training and testing sets. The training set consists of two-thirds

of the vectors from patients 1, 7, 9, 11, 15, 19, 21, 23, 25, 29 and 31 and negatives 2, 3, 4, 5, 6, 7, 8, 9, 11, 13 and 15; the test set is integrated by the remaining vectors. The SVM produces a prediction for each vector of the test set to be either uninfected or infected.

### Clinical samples and ethics statement

We obtained saliva samples through University Health Network's PRE-SERVE Pandemic Response Biobank (UHN REB 20-5364 and McGill IRB no. A03-M24-21B). The 33 SARS-CoV-2 clinical samples were collected from adult patients with COVID-19 symptoms such as fever, fatigue and dry cough. All samples were deidentified and tested positive for SARS-CoV-2 using RT-PCR. Moreover, the viral load was evaluated by qPCR (QuantStudio 12K Flex, Thermo Fisher Scientific). The qPCR primer sequences are provided in Supplementary Table 13. The samples were assessed at a Level 2+ facility situated in the Lady Davis Institute at the Jewish General Hospital.

### Electrochemical measurements

Electrochemical measurements were performed in a conventional three-electrode cell using an Autolab PGSTAT204 potentiostat/galvanostat. The plasmonic platforms were used as the working electrode, while Ag/AgCl and platinum wire served as the reference and counter electrodes, respectively. The potential of cyclic voltammetry tests ranged from  $-1$  to  $1$  V compared to the reference electrode with a scan rate of  $50 \text{ mV s}^{-1}$ . Measurement of the photoresponse was done by employing the chronoamperometry technique under chopped ambient visible light (light on–off cycles, 5 s) at a bias potential of  $1$  V versus Ag/AgCl in an aqueous nucleic acid amplification assay solution (10 parts LAMP Master Mix, 2 parts  $\times 10$  primer stock, 7 parts RNase-free water and 1 part target RNA sample).

### Characterization

For optimization studies on the plasmonic platforms, physical characterization techniques including atomic force microscopy (AFM) and SEM were employed. AFM was performed with Bruker MultiMode8 equipment while SEM was performed using an FEI Quanta 450 environmental scanning electron microscope.

The optical characterizations were performed via Lambda750 near-infrared–UV–visible equipment where measurements of the white light absorption during 60 min of amplification were collected from 200 nm to 850 nm. The study setting comprised the accumulation of the time point solutions on the platform where the incident and collected light beams had normal incidence to the platform. The fundamental electric-field distribution of the platform was studied using the finite-difference time-domain module (v.8.21.1781, Lumerical Solutions). The fundamental fluid flow and heat transfer characteristics of the microfluidic cartridge were studied using COMSOL Multiphysics (v.5.6).

### Statistical analysis

Results are conferred as the mean value  $\pm$  standard error of the mean for triplicate measurements as explained in the image processing section. The OriginPro (OriginLab, 2021) software package was used for statistical analysis. Limits of detection and linear ranges were calculated using linear regression methods, including the line slope and the standard error of the intercept. Statistical significance was evaluated using a one-way analysis of variance (ANOVA) with post hoc Tukey's test for mean comparison. Dataset difference was considered statistically significant for  $P < 0.001$ . The Paired Comparison Plot (v.3.60, OriginLab) graphing application was used to generate the figures using conservative  $P$  values.

### Reporting summary

Further information on research design is available in the Nature Portfolio Reporting Summary linked to this article.

### Data availability

The data supporting the results of this study are available within the paper and its Supplementary Information. The raw datasets generated and analysed during the study are available from the corresponding author upon reasonable request. Source data are provided with this paper.

### Code availability

The code for image processing is available on GitHub at <https://github.com/saramahshid/Nanoplasmonic-amplification>.

### References

- National Center for Biotechnology Information. *Basic Local Alignment Search Tool (BLAST)* <https://blast.ncbi.nlm.nih.gov/Blast.cgi> (NIH, 2023).
- CoVariants. *Shared Mutations* <https://covariants.org/shared-mutations> (2023).
- Hill, J. et al. Loop-mediated isothermal amplification assay for rapid detection of common strains of *Escherichia coli*. *J. Clin. Microbiol.* **46**, 2800–2804 (2008).
- Chen, X. et al. The rapid and visual detection of methicillin-susceptible and methicillin-resistant *Staphylococcus aureus* using multiplex loop-mediated isothermal amplification linked to a nanoparticle-based lateral flow biosensor. *Antimicrob. Resist. Infect. Control* **9**, 111 (2020).
- del Real Mata, C., Siavash Moakhar, R., Hosseini, I. I., Jalali, M. & Mahshid, S. A nanostructured microfluidic device for plasmon-assisted electrochemical detection of hydrogen peroxide released from cancer cells. *Nanoscale* **13**, 14316–14329 (2021).
- Jalali, M. et al. A hierarchical 3D nanostructured microfluidic device for sensitive detection of pathogenic bacteria. *Small* **14**, e1801893 (2018).
- Jalali, M. et al. Plasmonic nanobowtiefluidic device for sensitive detection of glioma extracellular vesicles by Raman spectrometry. *Lab Chip* **21**, 855–866 (2021).
- Innocenzi, P. et al. Hierarchical mesoporous films: from self-assembly to porosity with different length scales. *Chem. Mater.* **23**, 2501–2509 (2011).
- Sergyan, S. in *2008 6th International Symposium on Applied Machine Intelligence and Informatics* 221–224 (IEEE, 2008).
- Shahriari, B., Swersky, K., Wang, Z., Adams, R. P. & de Freitas, N. Taking the human out of the loop: a review of Bayesian optimization. *Proc. IEEE* **104**, 148–175 (2016).

### Acknowledgements

We thank the Faculty of Engineering at McGill University, Natural Sciences and Engineering Research Council of Canada (NSERC Alliance, 258928; G247765), Canadian Institutes of Health Research (257352), Canada Foundation for Innovation (G248924), MI4 Emergency COVID-19 Research Funding (250611) and MI4 Seed Fund Grant (256636) for financial support. S.M. and S.M.V. acknowledge financial support from the Canada Research Chairs Program. We acknowledge the Coronavirus Variants Rapid Response Network (CoVaRR-Net) for facilitating the acquisition of SARS-CoV-2 variant samples and N. M. Markarian for stock amplification and virus RNA preparation. We acknowledge the McGill University Health Centers containment level 3 platform, M. Behr and F. MacIntoch for supporting the project. We thank S. Sadat Mahshid for advice on clinical validation. We acknowledge Nanotools-Microfab at McGill University, Z. Lu and the research facilities of NanoQAM at the Université du Québec à Montréal. We acknowledge Nikon Canada, H. Saad and R. Battye for advice on the design and implementation of the imaging system. T.A., M.J. and C.d.R.M. acknowledge a FRQNT doctoral fellowship. T.A., M.J., C.d.R.M., R.S.M., S.G.Y. and I.I.H. acknowledge

support from the Faculty of Engineering for the MEDA award. This publication was supported by University Health Network's PRESERVE Pandemic Response Biobank for coronavirus samples, University Health Network's Biospecimen Services (UHN REB 20-5364 and McGill IRB # A03-M24-21B). Its contents are solely the responsibility of the authors and do not necessarily represent the official views of the University Health Network.

## Author contributions

S.M., T.A. and M.J. contributed to the idea conception. T.A., M.J., H.K., C.d.R.M., S.V.H., S.G.Y. and R.S.M. contributed to the design, planning and execution of the investigation. M.J., O.J., C.d.R.M. and H.K. contributed to the data analysis. M.J. and C.d.R.M. contributed to the design and fabrication of the plasmonic platforms. T.A., S.G.Y. and I.I.H. contributed to the fabrication of the microfluidic device. S.G.Y. and I.I.H. contributed to the design and execution of the imaging box. M.J. contributed to the theoretical study using finite-difference time-domain simulations and mechanistic calculations. S.G.Y. contributed to COMSOL numerical simulations. R.S.M. and M.J. contributed to the electrochemical studies and analysis. C.L. and S.M.V. contributed to the acquisition of patient samples, provided lab resources and materials at the hospital and contributed to writing the manuscript. D.N. and G.M. contributed to the bacteria sample preparation, testing and analysis, and contributed to the preparation of the manuscript. T.A. and M.M. contributed to performing RT-LAMP

tests at the Montreal Jewish General Hospital. M.M., Z.W. and D.P. contributed to the running of traditional qPCR analysis for SARS-CoV-2 samples. T.A., M.J., S.V.H., S.G.Y., C.d.R.M., O.J. and S.M. contributed to the preparation of the manuscript with the support and collaboration of all coauthors. S.M. supervised the project and contributed to the project conception, design of the experiments, interpretation of results, resources and funding acquisition.

## Competing interests

The authors declare no competing interests.

## Additional information

**Supplementary information** The online version contains supplementary material available at <https://doi.org/10.1038/s41565-023-01384-5>.

**Correspondence and requests for materials** should be addressed to Sara Mahshid.

**Peer review information** *Nature Nanotechnology* thanks Nikhil Bhalla and the other, anonymous, reviewer(s) for their contribution to the peer review of this work.

**Reprints and permissions information** is available at [www.nature.com/reprints](http://www.nature.com/reprints).

## Reporting Summary

Nature Portfolio wishes to improve the reproducibility of the work that we publish. This form provides structure for consistency and transparency in reporting. For further information on Nature Portfolio policies, see our [Editorial Policies](#) and the [Editorial Policy Checklist](#).

### Statistics

For all statistical analyses, confirm that the following items are present in the figure legend, table legend, main text, or Methods section.

n/a Confirmed

- |                                     |                                     |  |
|-------------------------------------|-------------------------------------|--|
| <input type="checkbox"/>            | <input checked="" type="checkbox"/> | The exact sample size ( $n$ ) for each experimental group/condition, given as a discrete number and unit of measurement  |
| <input type="checkbox"/>            | <input checked="" type="checkbox"/> | A statement on whether measurements were taken from distinct samples or whether the same sample was measured repeatedly  |
| <input type="checkbox"/>            | <input checked="" type="checkbox"/> | The statistical test(s) used AND whether they are one- or two-sided<br><i>Only common tests should be described solely by name; describe more complex techniques in the Methods section.</i>   |
| <input checked="" type="checkbox"/> | <input type="checkbox"/>            | A description of all covariates tested   |
| <input type="checkbox"/>            | <input checked="" type="checkbox"/> | A description of any assumptions or corrections, such as tests of normality and adjustment for multiple comparisons  |
| <input type="checkbox"/>            | <input checked="" type="checkbox"/> | A full description of the statistical parameters including central tendency (e.g. means) or other basic estimates (e.g. regression coefficient) AND variation (e.g. standard deviation) or associated estimates of uncertainty (e.g. confidence intervals) |
| <input type="checkbox"/>            | <input checked="" type="checkbox"/> | For null hypothesis testing, the test statistic (e.g. $F$ , $t$ , $r$ ) with confidence intervals, effect sizes, degrees of freedom and $P$ value noted<br><i>Give <math>P</math> values as exact values whenever suitable.</i>                            |
| <input checked="" type="checkbox"/> | <input type="checkbox"/>            | For Bayesian analysis, information on the choice of priors and Markov chain Monte Carlo settings   |
| <input type="checkbox"/>            | <input checked="" type="checkbox"/> | For hierarchical and complex designs, identification of the appropriate level for tests and full reporting of outcomes   |
| <input type="checkbox"/>            | <input checked="" type="checkbox"/> | Estimates of effect sizes (e.g. Cohen's $d$ , Pearson's $r$ ), indicating how they were calculated   |

Our web collection on [statistics for biologists](#) contains articles on many of the points above.

### Software and code

Policy information about [availability of computer code](#)

Data collection The finite difference time domain (FDTD) module (v8.21.1781, Lumerical Solutions, Inc.), Python 3.7.0, COMSOL Multi physics 5.6, Nova 2.1.5

Data analysis Origin Pro 2021b, Nova 2.1.5, Python 3.7.0, Arduino IDE 2.0.3 and MIT app inventor (no version number)

For manuscripts utilizing custom algorithms or software that are central to the research but not yet described in published literature, software must be made available to editors and reviewers. We strongly encourage code deposition in a community repository (e.g. GitHub). See the Nature Portfolio [guidelines for submitting code & software](#) for further information.

### Data

Policy information about [availability of data](#)

All manuscripts must include a [data availability statement](#). This statement should provide the following information, where applicable:

- Accession codes, unique identifiers, or web links for publicly available datasets
- A description of any restrictions on data availability
- For clinical datasets or third party data, please ensure that the statement adheres to our [policy](#)

The data supporting the results of this study are available within the paper and its Supplementary Information. The raw datasets generated and analyzed during the study are available from the corresponding authors upon reasonable request. Source data are provided with in this paper.



## Research involving human participants, their data, or biological material

Policy information about studies with [human participants or human data](#). See also policy information about [sex, gender \(identity/presentation\)](#), [and sexual orientation](#) and [race, ethnicity and racism](#).

### Reporting on sex and gender

The SARS-CoV-2 clinical patient samples obtained through University Health Network's PRESERVE-Pandemic Response Biobank. The patient samples were de-identified. Thus, we didn't have sex and gender information of the people providing the clinical samples.

### Reporting on race, ethnicity, or other socially relevant groupings

The collection of clinical patient samples was done in randomized fashion through University Health Network's PRESERVE-Pandemic Response Biobank and the patient samples were de-identified. Thus, we didn't have race, ethnicity or other socially relevant groupings information of the people providing the clinical samples.

### Population characteristics

University Health Network's PRESERVE-Pandemic Response Biobank collected SARS-CoV-2 clinical samples from adult patients with COVID-19 symptoms such as fever, fatigue, and dry cough.

### Recruitment

SARS-CoV-2 clinical samples were collected from adult patients with COVID-19 symptoms such as fever, fatigue, and dry cough through University Health Network's PRESERVE-Pandemic Response Biobank (IRB # A03-M24-21B). All samples were deidentified and tested positive for SARS-CoV-2 using RT-PCR.

### Ethics oversight

McGill Research Ethics Office (Institutional Review Board, A03-M24-21B).

Note that full information on the approval of the study protocol must also be provided in the manuscript.

## Field-specific reporting

Please select the one below that is the best fit for your research. If you are not sure, read the appropriate sections before making your selection.

☒ Life sciences

☐ Behavioural & social sciences

☐ Ecological, evolutionary & environmental sciences

For a reference copy of the document with all sections, see [nature.com/documents/nr-reporting-summary-flat.pdf](https://www.nature.com/documents/nr-reporting-summary-flat.pdf)

## Life sciences study design

All studies must disclose on these points even when the disclosure is negative.

### Sample size

For spiked SARS-CoV-2 we opted to cover the literature reported physiological concentration range thus covering the range from 8E5 to 5 RNA copies/ $\mu$ l in 10 fold concentrations for both RT LAMP and RCA assays. we opted to match the same scale for the Influenza A H1N1 virus testing in RT LAMP. For spiked bacteria experiments (E coli and MRSA) over the literature reported physiological concentration range thus covering the range from 7.2 to 7.2x10<sup>6</sup> gDNA copies/ml and 1 to 1E5 gDNA copies/ml. For SARS CoV-2 clinical samples due to the limited availabilities of samples we were able to secure 33 SARS-CoV-2 positive samples and 15 samples from uninfected people.

### Data exclusions

We didn't exclude data. Only outlier reads were automatically removed by our analysis python code, written by our group using available python libraries. The code cropped the outer perimeter of the raw images, subdivided each image into 20 mini images, removed imperfections and outliers\*, and finally extracting the RGB color values. (\*Thresholding implemented for values outside the color change range, fuchsia to yellow, due to possible inconsistencies in the formation of the self-assembly monolayer in the fabrication of QolorEX Nano platform).

### Replication

For spiked experiments we obtained 3 reads per condition time point. For patient samples we did the experiments 3 times each with 3 reads per condition time point. All of the experiments were reproducible.

### Randomization

he collection of clinical patient samples was done in randomized fashion since we obtained SARS-CoV-2 positive samples for random adult patients (through University Health Network's PRESERVE-Pandemic Response Biobank) as well as we acquired uninfected human samples from random individuals (through commercial sources -described in methods section).

### Blinding

The clinical patient samples were not blinded since they were already characterized as being SARS-CoV-2 positive or negative samples. Yet, the quantitative aspect (viral load per sample) was blinded since the RT-qPCR evaluation of the sample viral load was carried out after sample testing has been concluded.

## Reporting for specific materials, systems and methods

We require information from authors about some types of materials, experimental systems and methods used in many studies. Here, indicate whether each material, system or method listed is relevant to your study. If you are not sure if a list item applies to your research, read the appropriate section before selecting a response.

Materials & experimental systems

n/a	Involved in the study
<input checked="" type="checkbox"/>	<input type="checkbox"/> Antibodies
<input checked="" type="checkbox"/>	<input type="checkbox"/> Eukaryotic cell lines
<input checked="" type="checkbox"/>	<input type="checkbox"/> Palaeontology and archaeology
<input checked="" type="checkbox"/>	<input type="checkbox"/> Animals and other organisms
<input checked="" type="checkbox"/>	<input type="checkbox"/> Clinical data
<input checked="" type="checkbox"/>	<input type="checkbox"/> Dual use research of concern
<input checked="" type="checkbox"/>	<input type="checkbox"/> Plants

Methods

n/a	Involved in the study
<input checked="" type="checkbox"/>	<input type="checkbox"/> ChIP-seq
<input checked="" type="checkbox"/>	<input type="checkbox"/> Flow cytometry
<input checked="" type="checkbox"/>	<input type="checkbox"/> MRI-based neuroimaging